CHALMERS

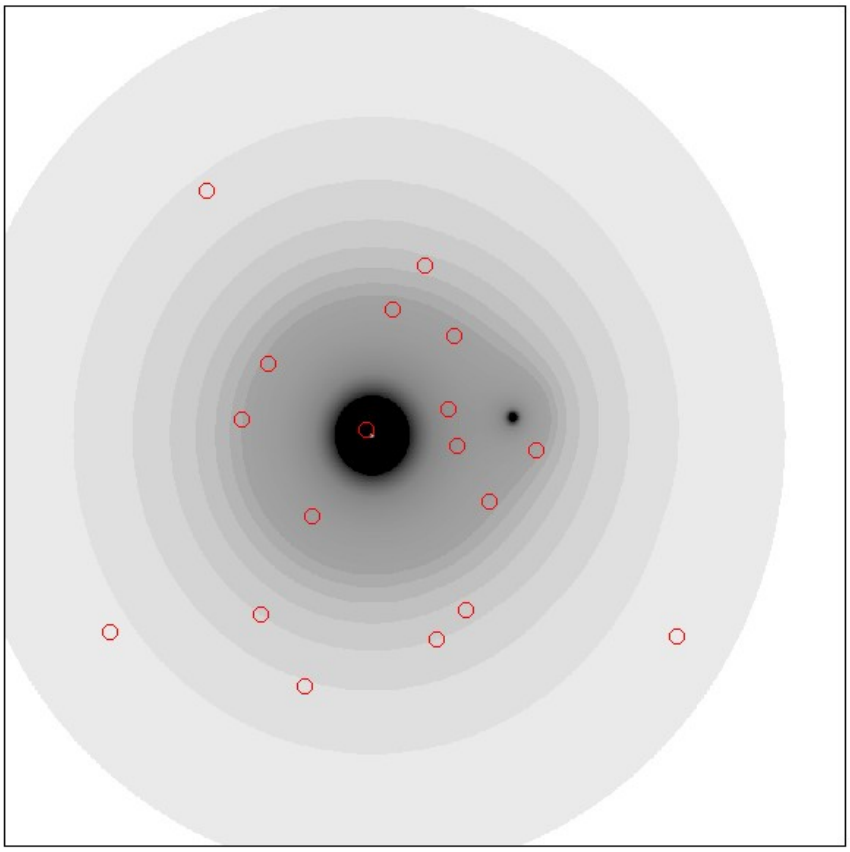

Gravitational lensing by galaxy clusters

Master of Science Thesis

HAUKUR SIGURDARSON

Department of Earth and Space Sciences
CHALMERS UNIVERSITY OF TECHNOLOGY
Göteborg, Sweden, 2010

Gravitational lensing by galaxy clusters

HAUKUR SIGURDARSON

Supervisor: CATHY HORELLOU

Department of Earth and Space Sciences

CHALMERS UNIVERSITY OF TECHNOLOGY

Göteborg, Sweden 2010

Gravitational lensing by galaxy clusters
HAUKUR SIGURDARSON

Department of Earth and Space Sciences
Chalmers University of Technology
SE-412 96 Göteborg
Sweden
Telephone +46 (0)31-772 1000

Cover:
A magnification map of the Bullet Cluster with the positions of submm sources marked with red circles

Contents

1 Introduction **2**

2 Submillimeter galaxies **3**

3 Theory of gravitational lensing **5**

3.1 Radially symmetrical lenses 7

3.2 The point-mass lens 8

3.3 The singular isothermal sphere (SIS) lens model 9

3.4 The Navarro-Frenk-White (NFW) lens model 10

3.5 Multiple lenses 12

4 The program **14**

5 The cluster models **15**

5.1 Abell 2163 15

5.2 1E 0657-56 16

5.3 Abell 2744 16

5.4 AC 144 16

5.5 MS 1054-03 17

5.6 Effects of errors in mass on the magnification 17

5.7 Effects of redshift on the magnification 18

6 Observations and data reduction **18**

7 Number counts **19**

8 Conclusion and discussion **21**

Abstract. Massive galaxy clusters can be utilized as giant natural telescopes; they magnify background galaxies giving us a view into the population of low flux density galaxies at high redshifts. Observations of such lensed galaxies require knowledge of the mass distribution of the lens in order to estimate the magnification of detected sources. In this work we present a computer program that simulates galaxy clusters as a superposition of spherically symmetric components represented by Navarro, Frenk & White (NFW) mass profiles and generates magnification maps. Those maps can be used to interpret observations of the (magnified) flux density of sources in cluster fields and to estimate the intrinsic flux density of the sources. We also discuss a way to correct for the effects of gravitational lensing in the analysis of number counts of submm galaxies that lie behind gravitational lenses.

1. Introduction

Gravitational lensing provides an opportunity to probe far out in space and time. By magnifying the apparent brightness of weak sources it allows us to study objects that would be impossible to detect without the lensing.

Massive galaxy clusters at intermediate redshifts ($z < 1$) are excellent candidates for gravitational lenses and have been used in a number of surveys in the submm waveband, the most comprehensive of which is the one by Knudsen et al. (2008) which probed far into the sub-mJy flux region, a region normally within the noise.

Without knowing the mass distribution of the lenses we cannot know which detected sources are lensed or by how much; a source with a high apparent flux could in reality be a faint source that is highly magnified by a gravitational lens.

In this work we present a program to simulate the lensing properties of clusters in order to estimate the magnification of sources detected behind massive galaxy clusters.

This work is organized as follows: in Part 2 the distant submillimeter galaxies are introduced along with a short discussion on some of their features; Part 3 of this work provides a short review of the theory of gravitational lensing upon which the rest of the work is built; in Part 4 the computer program used to calculate the magnification maps is discussed; in Part 6 observations of the five galaxy clusters used in this survey are presented; the effects of gravitational lensing on number counts are discussed in part 7 and Part 8 contains the conclusions and discussion.

We assume a cosmology with a Hubble parameter $H_0 = 70$ km Mpc^{-1} s^{-1}, a dark energy density parameter $\Omega_\lambda = 0.7$, a matter density parameter $\Omega_m = 0.3$ and an equation-of-state parameter of dark energy $\omega = -1$.

2. Submillimeter galaxies

Recent advances in sub-millimeter instruments have led to the discovery of a background of sub-millimeter galaxies.

Those galaxies are luminous high-redshift galaxies which are responsible for a major part of the energy released by all galaxies over the history of the Universe Blain et al. (2002).

The physical processes that control stellar, galactic and cosmological evolution, such as general relativity, gas dynamics and nuclear physics are relatively well understood but the initial conditions of the universe are less so. Studying the high-redshift population of galaxies allows us to restrain some of the boundary conditions of current cosmological models since it gives us a direct view of galaxy formation in the early universe.

High-redshift galaxies as those discussed in this paper cannot currently be studied with an angular resolution that allows us to detect their substructure. Studies of low-redshift galaxies have to be used to infer properties of more distant galaxies believed to be similar in nature. An example of well-studied galaxies that may have similar physical properties as the distant submm galaxies are the ultraluminous infrared galaxies (ULIRGs). They are defined by their high dust emission dominated luminosity, typically exceeding $10^{12} L_{\odot}$ when integrated over the dust dominated portion (corresponding to wavelengths of about 8μm - 1 mm) of the spectral energy distribution (SED).

The submm regime presents a number of challenges which have conspired to make it possible to study cosmology in the submm waveband only recently. Atmospheric emission and absorption makes it necessary to build telescopes on high and dry mountains or launch instruments into space. Sensitive receivers are hard to make in the boundary between radio-type coherent and optical-like incoherent detection techniques. Even then, the long wavelength of submm radiation sets a limit on the resolution we can get unless we use very large apertures. The largest single apertures available, which are in the 10-30 m class, provides angular resolution of the order of 10 arcseconds while optical instruments can reach a sub-arcsecond resolution.

The emission from galaxies in the submm regime is mostly made up of continuum emission from dust and line emissions from molecules in the interstellar medium.

The source that heats up the dust in order for it to emit radiation in these galaxies is often not known. Intense optical or UV sources such as young stars or active galactic nuclei (AGN) could supply the energy but since the dust emits a featureless blackbody spectrum little information can be gained from it.

In ULIRGs where the internal structure has been resolved, the dust emission comes from a small sub-kpc central regions in mergers possibly due to AGN activity shrouded by thick gas and dust (e.g. Downes & Solomon 1998; Sakamoto et al. 1999) or a central starburst fed by a bar instability (e.g Mihos 1999).

The regions of galaxies obscured by dust and gas can be probed by near- and mid-IR spectroscopy where the optical depth is less than in the optical and UV bands. A study performed using the *Infrared*

Space Observatory (ISO) suggested that most of the low-redshift ULIRGs are driven by high star forming activity. They also found that the more luminous a ULIRG is the more likely it is powered by an AGN (Sanders 1999). Since most of the high redshift ULIRGs are more luminous than those in the local Universe this could be an important factor.

At submm wavelengths the SED of the galaxies increase strongly with frequency, so when we observe highly redshifted sources we measure closer to the peak of their SED. This counteracts the decrease in luminosity due to larger distances. In practice, this has the effect that at submm wavelengths galaxies with redshift between 1 and 20 have similar measured flux densities, independent of redshift. This so-called negative K-correction applies to wavelengths greater than $250\mu m$ Hogg et al. (2002).

The K-correction has the adverse effect of making it impossible to estimate the redshift of submm galaxies from single wavelength submm flux densities. The difficulty in precise positioning of submm sources further complicates finding optical counterparts for spectroscopy.

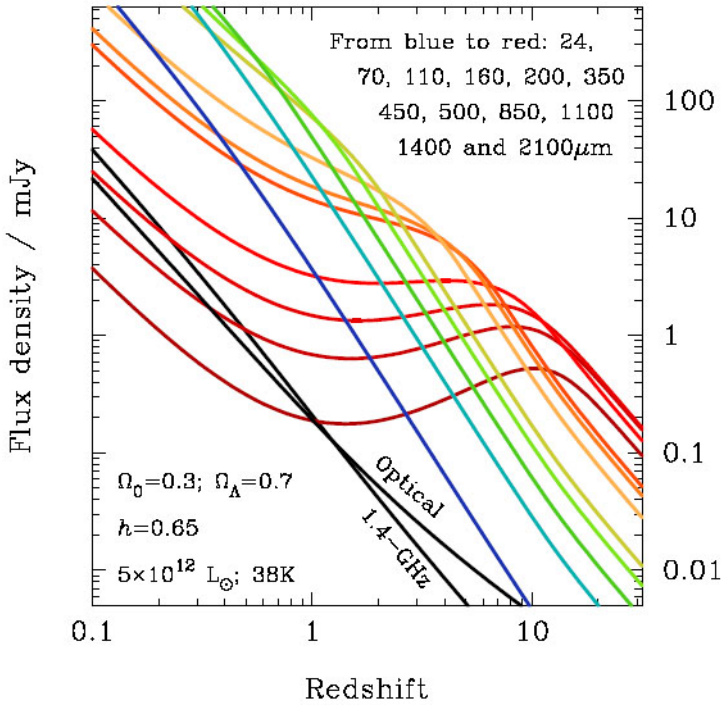

Fig. 1.—: The predicted flux density of a dusty galaxy at various submm wavelengths. At a wavelength above 250μm the flux density is almost independent of redshift due to the strong K-correction. Figure from Blain et al. 2002

A number of submm surveys have been performed of low- to mid-redshift (z<1) galaxy clusters in order to exploit the effect of gravitational lensing which magnifies the flux of high redshift galaxies making them easier to detect. The submm band has the added benefit that the foreground galaxies that make up the cluster itself contribute little to the detected flux, so the sources found are likely to be distant galaxies. The survey discussed in this work is composed of five such fields where galaxy clusters with redshifts in the 0.2-0.8 range lens background galaxies at higher redshifts.

Notable sub-mm instruments include the Submillimetre User Bolometer Array (SCUBA) at the

James Clerk Maxwell Telescope (JCMT) (Holland et al. 1999) which images in the 450μm and 850μm bands using 91 and 31 bolometers in an hexagonal array.

The instrument used for the observations in this work is the Large APEX Bolometer Camera (LABOCA) at the Atacama Pathfinder EXperiment (APEX) in Chile. It operates at a wavelength 870 μm with 295 bolometers.

Looking towards the future, the Atacama Large Millimeter Array (ALMA), which is being constructed and will consist of a total of 66 12-meter and 7-meter telescopes, will offer a major increase in detection capabilities in the submm regime. When fully operational it will provide a resolution of up to 10 micro-arcseconds, allowing for the study of substructure in high-redshift galaxies.

3. Theory of gravitational lensing

As a ray of light passes by a massive object such as a cluster of galaxies it deviates from its trajectory due to the curvature of spacetime. The new trajectory will form an angle of deflection α with the initial direction of the ray. The magnitude of α for a spherically symmetric mass was first calculated by Einstein (1936) and is

$$\hat{\alpha} = \frac{4GM}{c^2\xi} \tag{1}$$

where M is the mass of the object which causes the deflection, ξ is the impact parameter of the incoming light ray, G is the gravitational constant and c the speed of light. Here it is assumed that the ray impact parameter is much larger than the Schwarzschild radius of the deflecting mass, $\xi \gg R_{\rm S} \equiv 2GMc^{-2}$.

This condition means that the deflection angle is small, which in turn implies that the gravitational field is weak and that the field equations of General Relativity can be linearized (Schneider et al. 2006). The total deflection angle is then a simple sum of the deflection angles from a ensemble of point masses.

We consider a mass distribution with density $\rho(\boldsymbol{r})$ divided into infinitesimal volume elements dV each with a mass $dm = \rho(\boldsymbol{r})dV$.

A light ray passing by this mass distribution has a trajectory that can be expressed as an affine parametrization $(\xi_1(\lambda), \xi_2(\lambda), r_3(\lambda))$ with an affine parameter λ and in coordinates chosen so that the ray propagates along r_3 when far from the mass distribution.

By assuming a thin lens (that is a mass distribution that extends a relatively short distance parallel to the light ray compared to the distance from the source to the observer, a valid assumption when discussing galaxy clusters), then $\boldsymbol{\xi}(\lambda) \approx \boldsymbol{\xi} = (\xi_1, \xi_2)$, independent of the affine parameter λ.

This allows us to express the impact vector of a light ray at $\boldsymbol{\xi}$ relative to a mass element at $\boldsymbol{r}' = (\xi_1', \xi_2', r_3')$ as $(\xi) - (\xi)'$, independent of r_3' and thus the total deflection angle is

$$\hat{\boldsymbol{\alpha}}(\boldsymbol{\xi}) = \frac{4G}{c^2} \int d^2\xi' \int dr_3' \rho(\xi_1', \xi_2', r_3') \frac{\boldsymbol{\xi} - \boldsymbol{\xi}'}{|\boldsymbol{\xi} - \boldsymbol{\xi}'|^2} \, . \tag{2}$$

the surface mass density is defined as the mass density of the lens projected onto a plane perpen-

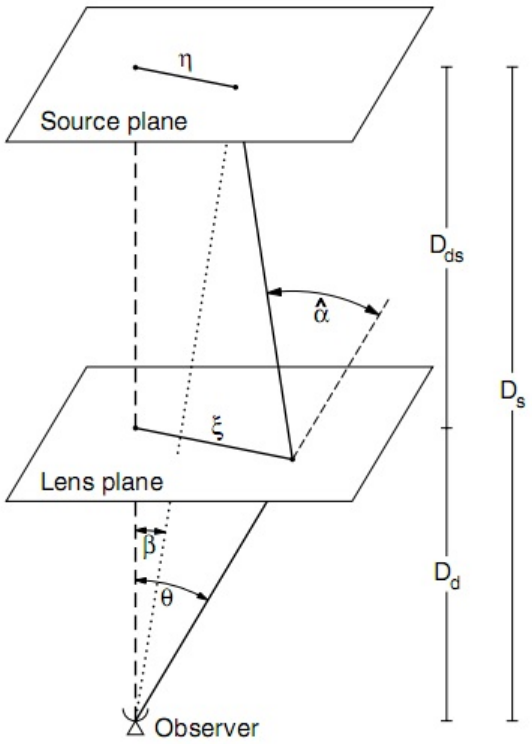

Fig. 2.—: Sketch of a typical gravitational lens system (Schneider et al. 2006)

dicular to the light ray and is written as

$$\Sigma(\boldsymbol{\xi}) \equiv \int dr_3 \rho(\xi_1, \xi_2, r_3) \ , \tag{3}$$

and so the deflection angle is

$$\hat{\boldsymbol{\alpha}}(\boldsymbol{\xi}) = \frac{4G}{c^2} \int d^2\xi' \Sigma(\boldsymbol{\xi}') \frac{\boldsymbol{\xi} - \boldsymbol{\xi}'}{|\boldsymbol{\xi} - \boldsymbol{\xi}'|^2} \ . \tag{4}$$

A typical lensing situation is depicted in figure 2 with a lens at a distance of $D_{\rm d}$ and a source at a distance $D_{\rm s}$ from the observer. The distances D with subscripts d,s and ds correspond to the three angular-diameter distances, observer-to-lens, observer-to-source and lens-to-source, respectively. In a similar way to regular optical geometry and recalling our assumption of a thin lens, the path of a ray of light from the source which is deflected by the lens can be approximated as two straight lines with a kink near the lens. In reality the path is smoothly curved near the lens. By reading of the geometric condition and assuming that all angles are small (a valid assumption considering the distance to a cluster compared to its size), we get the relation

$$\boldsymbol{\eta} = \frac{D_s}{D_d} \boldsymbol{\xi} - D_{ds} \hat{\boldsymbol{\alpha}}(\boldsymbol{\xi}) \ . \tag{5}$$

Using the angular coordinates $\boldsymbol{\eta} = D_s \boldsymbol{\beta}$ and $\boldsymbol{\xi} = D_d \boldsymbol{\theta}$ we can write the *lens equation* as

$$\boldsymbol{\beta} = \boldsymbol{\theta} - \frac{D_{ds}}{D_s} \hat{\boldsymbol{\alpha}}(D_d \boldsymbol{\theta}) \equiv \boldsymbol{\theta} - \boldsymbol{\alpha}(\boldsymbol{\theta}) \tag{6}$$

where

$$\boldsymbol{\alpha}(\boldsymbol{\theta}) = \frac{1}{\pi}\int_{\mathbb{R}^2} d^2\theta' \kappa(\boldsymbol{\theta}') \frac{\boldsymbol{\theta}-\boldsymbol{\theta}'}{|\boldsymbol{\theta}-\boldsymbol{\theta}'|^2} \tag{7}$$

is the scaled deflection angle,

$$\kappa(\boldsymbol{\theta}) \equiv \frac{\Sigma(D_d\boldsymbol{\theta})}{\Sigma_{cr}} \tag{8}$$

is the convergence and

$$\Sigma_{\rm cr} = \frac{c^2}{4\pi G}\frac{D_s}{D_d D_{ds}} \tag{9}$$

is the critical surface mass density. The lens equation (1) shows how the observed position of a source relates to the real position of the source and the deflection due to the lens. A mass distribution that has $\Sigma \geq \Sigma_{\rm cr}$ will produce multiple images of a single source. Such a lens is referred to as a strong lens and equation (1) will have multiple solutions for a fixed $\boldsymbol{\beta}$.

The distortion of images can be described by the Jacobian of the lens equation

$$\mathcal{A}(\boldsymbol{\theta}) = \frac{\partial\boldsymbol{\beta}}{\partial\boldsymbol{\theta}} = \begin{pmatrix} 1-\kappa-\gamma_1 & -\gamma_2 \\ -\gamma_2 & 1-\kappa+\gamma_1 \end{pmatrix} \tag{10}$$

where

$$\gamma_1 = \frac{1}{2}(\psi_{,11}-\psi_{,22}) \qquad \gamma_2 = \psi_{,12}\ , \tag{11}$$

and γ is related to κ through the deflection potential ψ

$$\nabla^2\psi = 2\kappa\ . \tag{12}$$

The magnification factor can then be computed by taking the determinant of the inverse of the Jacobian

$$\mu = \frac{1}{\det\mathcal{A}}\ . \tag{13}$$

3.1. Radially symmetrical lenses

For a mass distribution that is radially symmetric, that is $\Sigma(\boldsymbol{\xi}) = \Sigma(|\boldsymbol{\xi}|)$ one can rewrite equation (2)

$$\hat{\boldsymbol{\alpha}}(\boldsymbol{\xi}) = \frac{\boldsymbol{\xi}}{|\boldsymbol{\xi}|^2}\frac{4G}{c^2}2\pi\int_0^{\xi} d\xi'\xi'\Sigma(\xi') \equiv \frac{4GM(|\boldsymbol{\xi}|)}{c^2|\boldsymbol{\xi}|^2}\boldsymbol{\xi} \tag{14}$$

where $M(\xi)$ is the projected mass inside a radius of ξ. The deflection angle is thus the same as for a point mass with a total mass of $M(\xi)$ and mass outside the radius ξ has no effect on the deflection.

From equation (6) we can see that since $\boldsymbol{\alpha}$ is collinear with $\boldsymbol{\theta}$ (and $\boldsymbol{\xi}$) then so is $\boldsymbol{\beta}$ and the lens equation becomes one-dimensional

$$\beta = \theta - \alpha(\theta) \tag{15}$$

where

$$\alpha(\theta) = \frac{m(\theta)}{\theta} = \overline{\kappa}(\theta)\theta \tag{16}$$

and

$$m(\theta) = 2\int_0^\theta d\theta' \theta' \kappa(\theta') \tag{17}$$

is the dimensionless mass inside a circle of angular radius θ and

$$\overline{\kappa}(\theta) = \frac{m(\theta)}{\theta^2} \tag{18}$$

is the mean surface mass density inside the same circle. The lens equation can now be written as

$$\boldsymbol{\beta} = [1 - \overline{\kappa}(|\boldsymbol{\theta}|)]\boldsymbol{\theta} \tag{19}$$

and according to equation (10) the Jacobian is in this case expressed as

$$\mathcal{A}(\boldsymbol{\theta}) = [1 - \overline{\kappa}(|\boldsymbol{\theta}|)]\boldsymbol{I} - \frac{\overline{\kappa}'}{|\boldsymbol{\theta}|}\begin{pmatrix} \theta_1^2 & \theta_1\theta_2 \\ \theta_1\theta_2 & \theta_2^2 \end{pmatrix} \tag{20}$$

where $\boldsymbol{I}$ is the two-dimensional identity matrix, and $\overline{\kappa}' \equiv d\overline{\kappa}/d\theta = 2[\kappa(\theta) - \overline{\kappa}(\theta)]/\theta$.

3.2. The point-mass lens

The simplest lens model is that of a point-mass lens. In this case all the mass is concentrated in a single point. It is easily seen that such a distribution is spherically symmetric and we can use the results from the previous part to simplify things. Due to the fact that in a spherically symmetric lens only the mass inside a circle with radius ξ affects the deflection angle, the equations for a point-mass lens are also valid for any region outside a spherical mass distribution.

For a point-mass lens of mass M the surface mass density is $\Sigma(\boldsymbol{\xi}) = M\delta_D(\boldsymbol{\xi})$ where δ_D is the Dirac delta function. The deflection angle is then according to equation (2)

$$\hat{\boldsymbol{\alpha}}(\boldsymbol{\xi}) = \frac{4GM}{c^2}\frac{\boldsymbol{\xi}}{|\boldsymbol{\xi}|^2} \tag{21}$$

and the lens equation becomes

$$\boldsymbol{\beta} = \boldsymbol{\theta} - \frac{4GMD_{ds}}{c^2 D_D D_s}\frac{\boldsymbol{\theta}}{|\boldsymbol{\theta}|^2} = \boldsymbol{\theta} - \theta_{\mathrm{E}}^2 \frac{\boldsymbol{\theta}}{|\boldsymbol{\theta}|^2} \tag{22}$$

where

$$\theta_E = \frac{4GMD_{ds}}{c^2 D_D D_s} \tag{23}$$

is the so-called Einstein radius of the lens. This radius is the distance from the point-mass to the critical line, that is where the magnification tends to infinity. A source behind the center of the lens will be stretched into a ring with radius θ_E, an *Einstein ring*.

Consider a source on the positive β-axis, then $\boldsymbol{\theta}$ will also lie on the positive θ-axis and the lens equation becomes one-dimensional

$$x_{\pm} = \frac{1}{2}\left(y \pm \sqrt{y^2+4}\right) \ , \tag{24}$$

where $x = \theta/\theta_{\mathrm{E}}$ and $y = \beta/\theta_{\mathrm{E}}$ are the rescaled angles. It is apparent that this equation has two solutions for any arbitrary source position y, which means that any source will have two images, one on each side of the lens.

We can now calculate the magnification by finding that for a point-mass, $m(\theta) = \theta_{\mathrm{E}}^2$ and $\overline{\kappa}(\theta) = (\theta_{\mathrm{E}}/\theta)^2 = x^{-2}$, and so from equation (20) we get a magnification

$$\mu = \frac{1}{\det \mathcal{A}} = \frac{1}{1-\overline{\kappa}^2} = \left(1 - \frac{1}{x^4}\right)^{-1} . \tag{25}$$

From this equation it's easy to see that the magnification diverges towards infinity when x tends to 1, that is when $\theta = \theta_E$ and the image lies on a critical line.

A point mass lens model may be appropriate for a star or other compact object but for galaxies or clusters a more suitable model has to be used since then the angular size of the mass distribution is of a comparable size to changes in the deflection potential.

3.3. The singular isothermal sphere (SIS) lens model

Galaxies and galaxy clusters are not point-masses and a point-mass lens model is ill-suited to deduce their lensing properties. A simple model that can approximate the effects of a galactic or cluster lens is the so-called *singular isothermal sphere* (SIS). The density profile for such a SIS is

$$\rho(r) = \frac{\sigma_\nu^2}{2\pi G r^2} \tag{26}$$

where σ_ν is the one-dimensional velocity distribution of the constituent self-gravitating particles of which the lens is made of. The velocity distribution is Maxwellian at all radii, hence the 'isothermal' part of the name. This distribution yields flat rotation curves in accordance to those that are observed for spiral galaxies. Since the mass distribution has a singularity in the center it is not physical but this can

be remedied by introducing a finite core radius where the distribution is truncated. The mass also tends to infinity at large radii but this can be circumvented by considering only the lensing effects at smaller radii. For those reasons along with the development of better lensing models for galaxies and clusters the SIS is not used extensively anymore, but due to its simplicity it can be used in rough approximations.

The projected surface mass density of a SIS profile is

$$\Sigma(\xi) \int_{-\infty}^{\infty} dr_3 \rho \left(\sqrt{\xi^2 + r_3^2} \right) = \frac{\sigma_\nu^2}{2G} \xi^{-1} \tag{27}$$

yielding an Einstein radius of

$$\theta_{\rm E} = 4\pi \left(\frac{{\sigma_\nu}^2}{c} \right) \frac{D_{ds}}{D_s}. \tag{28}$$

Rescaling with the Einstein radius yields

$$\kappa(\theta) = \gamma|(\theta) = \frac{\theta_{\rm E}}{|\theta|}; \quad \overline{\kappa} = \frac{\theta_{\rm E}}{|\theta|}; \quad \alpha(\theta) = \theta_{\rm E} \frac{\theta}{|\theta|} \tag{29}$$

and the lens equation for a SIS can be written as

$$\beta = \theta - \theta_{\rm E} \frac{\theta}{|\theta|}. \tag{30}$$

Using the scaled angles $x = \theta/\theta_{\rm E}$ and $y = \beta/\theta_{\rm E}$ as in the previous section we get

$$y = x - \frac{x}{|x|} \, . \tag{31}$$

The magnification is then

$$\mu = \frac{1}{\det \mathcal{A}} = \frac{1}{1 - \overline{\kappa}} = \frac{|x|}{|x| - 1} \tag{32}$$

where it is again easily seen that critical lines lie on $|x| = 1$.

As mentioned in the beginning of this section: while the SIS model has the advantage of being very simple and still resulting in flat rotation curves, recent works prefer to use the model discussed in the next section.

3.4. The Navarro-Frenk-White (NFW) lens model

N-body simulations of hierarchical clustering of dark matter halos predicts a certain mass profile, the so called Navarro-Frenk-White (NFW) profile (Navarro et al. 1997). All cluster models in this work will use one or a superposition of NFW profiles both for consistency between clusters and because it is a popular model of mass distribution in the literature and thus mass estimates found for the clusters are often estimated by assuming a NFW profile.

The NFW profile is spherically symmetric and its density is described by the relation (Navarro et al. 1997)

$$\rho(r) = \frac{\rho_s}{(cr/r_{\rm vir})(1 + cr/r_{\rm vir})^2} \tag{33}$$

where $r_{\rm vir}$ is the virial radius of the halo and c is the halo concentration parameter.

The virial radius $r_{\rm vir}$ is related to the virial overdensity Δ_c and to the critical density at the redshift of the lens $\rho_{\rm crit}(z)$

$$r_{\rm vir} = \left(\frac{3M_{\rm vir}}{\rho_{\rm crit}(z) 4\pi \Delta_c} \right)^{1/3} \tag{34}$$

where

$$\rho_{\rm crit}(z) = \rho_{\rm crit}(0) \frac{H^2(z)}{H_0^2} = \rho_{\rm crit}(0) \left[\Omega_m (1+z)^3 + \Omega_\lambda (1+z)^{3(1+\omega)} \right] \tag{35}$$

in a flat Universe and Δ_c can be estimated by a fit to numerical simulations (Bryan & Norman 1998)

$$\Delta_c = 18\pi^2 + 82x - 39x^2 \tag{36}$$

where $x = \omega_m(z) - 1$ and $\omega_m(z) = \Omega_m (1+z)^3 H_0^2 / H^2(z)$.

The concentration parameter $c_{\rm vir}$ can be calculated using the virial mass through a fit to simulations (Bullock et al. 2001)

$$c_{\rm vir}(M_{\rm vir}, z) = \frac{9}{1+z} \left(\frac{M_{\rm vir}}{M_*} \right)^{-0.13} \tag{37}$$

with $M_* = 1.5 \times 10^{13} h^{-1} M_\odot$ and $h = H/(100 \text{ km s}^{-1}\text{Mpc}^{-1})$.

The surface density profile for the NFW profile is (Takada & Jain 2003)

$$\Sigma(\theta) = \int_{-r_{\rm vir}}^{r_{\rm vir}} dr_{||} \rho(r) = \frac{M_{\rm vir} f c^2}{2\pi r_{\rm vir}^2} F(c_{\rm vir}\theta/\theta_{\rm vir}) \tag{38}$$

where

$$F(x) = \begin{cases} -\frac{\sqrt{c_{\rm vir}^2 - x2}}{(1-x^2)(1+c_{\rm vir})} + \frac{1}{(1-x^2)^{3/2}} \text{arccosh} \frac{x^2 + c_{\rm vir}}{x(1+c_{\rm vir})} \ , & (x < 1) \\ \frac{\sqrt{c_{\rm vir}^2 - 1}}{3(1+c_{\rm vir})} \left[1 + \frac{1}{c_{\rm vir}+1} \right] \ , & (x = 1) \\ -\frac{\sqrt{c_{\rm vir}^2 - x^2}}{(1-x^2)(1+c_{\rm vir})} - \frac{1}{(x^2-1}^{3/2} \text{arccos} \frac{x^2 + c_{\rm vir}}{x(1+c_{\rm vir})} \ , & (x = 1) \\ 0 \ , & (x > c_{\rm vir}) \end{cases} \tag{39}$$

and $f = (\ln(1+c) - c/(1+c))^{-1}$ and $\theta_{\rm vir} = r_{\rm vir}/D_A$, where D_A is the angular-diameter distance. Using equations (39) and (8) the convergence field κ can be calculated.

The shear is computed in a similar way

$$\gamma(\theta) = \frac{M_{\rm vir} f c_{\rm vir}^2}{2\pi r_{\rm vir}^2} \frac{G(c_{\rm vir}\theta/\theta_{\rm vir})}{\Sigma_{\rm cr}} \tag{40}$$

where

$$G(x) = \begin{cases} \frac{1}{x^2(1-c_{\rm vir})} \left[\frac{(2-x^2)\sqrt{c_{\rm vir}^2 - x^2}}{1-x^2} - 2c_{\rm vir} \right] + \frac{2}{x^2} \ln \frac{x(1+c_{\rm vir})}{c_{\rm vir} + \sqrt{c_{\rm vir}^2 - x^2}} + \frac{2-3x^2}{x^2(1-x^2)^{3/2}} \text{arccosh} \frac{x^2 + c_{\rm vir}}{x(1+c_{\rm vir})} \ , & (x < 1) \\ \frac{1}{3(1+c_{\rm vir})} \left[\frac{(11c+10)\sqrt{c_{\rm vir}^2 - 1}}{1+c_{\rm vir}} - 6c_{\rm vir} \right] + 2 \ln \frac{1+c_{\rm vir}}{c_{\rm vir} + \sqrt{c_{\rm vir}^2 - 1}} \ , & (x = 1) \\ \frac{1}{x^2(1+c_{\rm vir})} \left[\frac{(2-x^2)\sqrt{c_{\rm vir}^2 - x^2}}{(1-x^2)} - 2c_{\rm vir} \right] + \frac{2}{x^2} \ln \frac{x((1+c_{\rm vir})}{c + \sqrt{c_{\rm vir}^2 - x^2}} - \frac{2-3x^2}{x^2(x^2-1)^{3/2}} \arccos \frac{x^2 + c_{\rm vir}}{x(1+c_{\rm vir})} \ , & (1 < x < c_{\rm vir}) \\ \frac{2f^{-1}}{x^2} \ . & (x > c_{\rm vir}) \end{cases} \tag{41}$$

With the equations for the convergence and the shear we can use (10) and (13) to calculate the magnification.

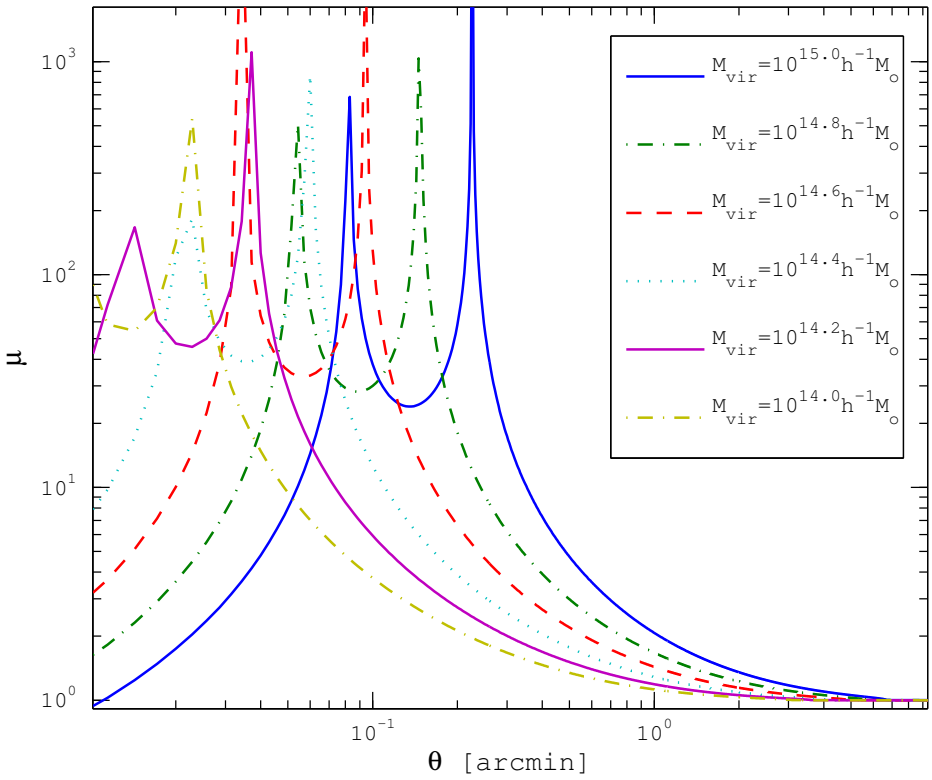

Fig. 3.—: The magnification as a function of the distance from the center of a NFW mass profile. Each curve represents a different virial mass, in all cases the lens is at redshift $z_l = 0.5$ and the source plane at $z = 2.0$. The figure was constructed by plotting the magnification along a cross section of magnification maps created by the computer program in section 4. This figure can be compared to figure 2 in Lima et al. 2010 where a similar figure is made by solving μ as a function of θ directly.

3.5. Multiple lenses

In the case of multiple lenses in the same plane, that is a lens described by multiple independent distributions of mass, the deflection angle is simply the superposition of the individual deflections (Bourassa et al. 1973)

$$\boldsymbol{\beta} = \boldsymbol{\theta} - \sum_n \boldsymbol{\alpha}_n(\boldsymbol{\theta}) \tag{42}$$

where we sum over n lenses. The Jacobian then becomes

$$\mathcal{A}(\boldsymbol{\theta}) = \frac{\partial \boldsymbol{\beta}}{\partial \boldsymbol{\theta}} = \left(\delta_{ij} - \sum_n \frac{\partial \psi_n(\boldsymbol{\theta})}{\partial \theta_i \partial \theta_j} \right) = \boldsymbol{I} - \sum_n \mathcal{B}_n \tag{43}$$

where

$$\mathcal{B} = \begin{pmatrix} -\kappa - \gamma_1 & -\gamma_2 \\ -\gamma_2 & -\kappa + \gamma_1 \end{pmatrix} \tag{44}$$

is the Jacobian of a single lens sans the identity matrix $\boldsymbol{I}$. As before the magnification can then be calculated using (13).

For a simple system such as the two-point-mass lens this can be solved analytically (Schneider & Weiss 1986). Schneider & Weiss considered two point mass lenses with masses M_1 and M_2. Using the same notation as in part 3 the deflection angle for this system is

$$\hat{\boldsymbol{\alpha}}(\boldsymbol{\xi}) = \frac{4GM_1}{c^2}\frac{\boldsymbol{\xi} - \boldsymbol{\rho}_1}{|\boldsymbol{\xi} - \boldsymbol{\rho}_1|^2} + \frac{4GM_2}{c^2}\frac{\boldsymbol{\xi} - \boldsymbol{\rho}_2}{|\boldsymbol{\xi} - \boldsymbol{\rho}_2|^2} \tag{45}$$

where $\boldsymbol{\rho}_1$ and $\boldsymbol{\rho}_2$ are the projection points of the two point masses onto the lens plane. Defining a characteristic length

$$\rho_0 = \sqrt{\frac{4GM}{c^2}\frac{D_d D_{ds}}{D_s}} \tag{46}$$

where $M = M_1 + M_2$ is the total mass of the system. (This length is the Einstein radius of a point mass of mass M). Further defining

$$\begin{aligned} \boldsymbol{r} &= \boldsymbol{\xi}/\rho_0\,, & (47)\\ \boldsymbol{x} &= (D_d/D_s)\cdot\boldsymbol{\eta}/\rho_0\,, & (48)\\ \mu_1 &= M_1/M, \quad \mu_2 = M_2/M, & (49)\\ & & (50) \end{aligned}$$

the lens equation can be rewritten as a function of $\boldsymbol{x}$ and $\boldsymbol{r}$

$$\boldsymbol{x} = \boldsymbol{r} - \boldsymbol{\alpha}(\boldsymbol{r}) \tag{51}$$

where

$$\boldsymbol{\alpha}(\boldsymbol{r}) = \mu_1\frac{\boldsymbol{r} - \boldsymbol{r}_0}{|\boldsymbol{r} - \boldsymbol{r}_0|^2} + \mu_2\frac{\boldsymbol{r} - \boldsymbol{r}_0}{|\boldsymbol{r} - \boldsymbol{r}_0|^2} \tag{52}$$

where the point masses are located at the points $\pm\rho_0\boldsymbol{r}_0$. Choosing coordinates so that $\boldsymbol{r}_0 = (X, 0)$, for an arbitrary constant $X \geq 0$ the determinant of the Jacobian is

$$\det\mathcal{A} = 1 - \left(\frac{\mu_1}{|\boldsymbol{r} - \boldsymbol{r}_0|^2} + \frac{\mu_2}{|\boldsymbol{r} - \boldsymbol{r}_0|^2}\right)^2 + \frac{16\mu_1\mu_2X^2r_0^2}{|\boldsymbol{r} - \boldsymbol{r}_0|^4|\boldsymbol{r} + \boldsymbol{r}_0|^4}. \tag{53}$$

Figure 4 displays a comparison between Schneider & Weiss 's analytical calculations and a magnification map constructed from directly solving equations (10) and (13). The latter method is the one that will be used extensively in this work.

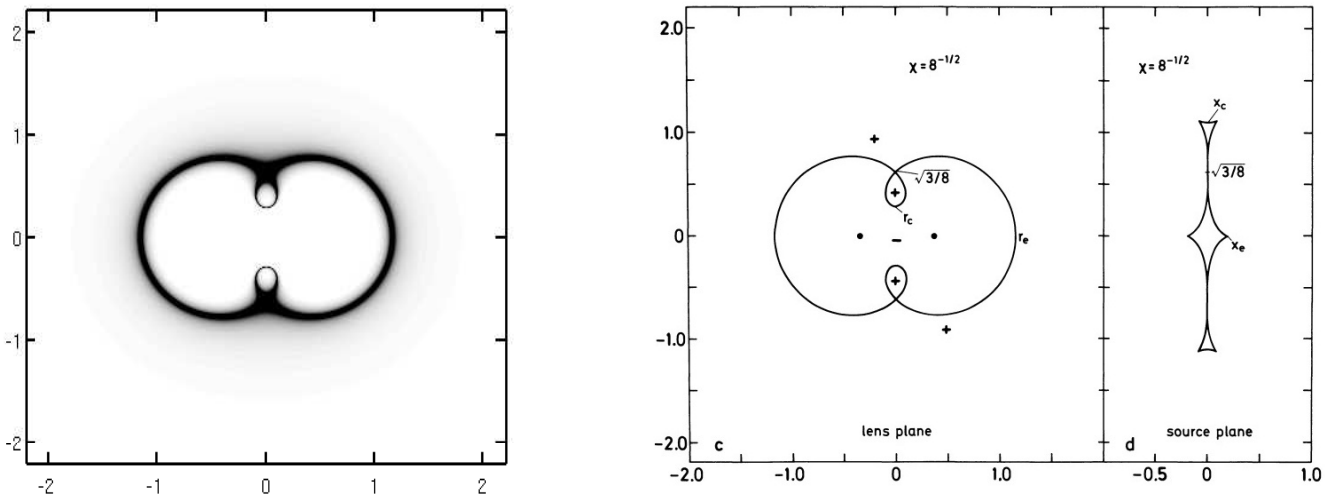

Fig. 4.—: A two-point mass system. Comparison of the magnification map constructed by numerically calculating the Jacobian at every point in the map (left) and Schneider's analytical solution (right) (Schneider & Weiss 1986). In both cases the distance between the lenses is the same. The figure on the left shows the absolute value of the magnification $|\mu|$ in the lens plane while on the right only the critical lines in the source plane and the corresponding caustics in the source plane are marked. The area of high magnification coincides with the critical lines where μ approaches infinity.

4. The program

To perform the calculations discussed in part 3 a Matlab program was written.

The program employs a straight-forward method in which a magnification map is made by inputting the parameters which make up a lens model. These parameters include the cosmological parameters in addition to the defining parameters of the lens itself. Each lens is assumed to be made up of one or more NFW mass profiles. For each NFW profile, a mass, redshift of the lens and the source plane and relative position from a center position is provided.

The program then makes a 2D map and calculates for each pixel the total Jacobian in equation (43) for all the profiles and through equation (13) the total magnification in the pixel.

A magnification map is made for each of the five fields using the cluster models discussed below. The sources detected in the LABOCA maps can then be positioned in the corresponding map and the magnification for each source can then be read of directly. Here we assume that the sources are point sources located at their centroid as measured from the LABOCA map, so only the magnification at the centroid is used as the real magnification of the source.

For reasons discussed in more detail in part 7 the program also calculates the total area of all five fields which has a magnification larger than a certain magnification μ and the area in the source plane corresponding to that area in the lens plane. This is done simply by counting the pixels with a certain μ

where each pixel corresponds to a certain area unit.

In our case we found that a 1500×1500 map provided a good compromise between resolution and computing time. Each map is 15×15 arcminutes making each pixel a 0.6×0.6 arcsecond square.

5. The cluster models

As mentioned above each cluster is modeled as one or more NFW profiles. Table 1 displays the relevant parameters for each cluster. A short discussion of the clusters follows.

Table 1:: Cluster model parameters. Included are the redshift of the cluster, the mass of each component, the relative positions of the components, the concentration parameter c as calculated from equation (37) and the angular scale radius $R_s = R_{\rm vir}/c$.

Cluster	Redshift	Mass [$10^{14} M_\odot$]	Rel. pos. [$''$]	c	R_s [$'$]	References
Abell 2163	0.203	22±0.4	0,0	3.7	4.2	Radovich et al. (2008)
1E 0657-56	0.296	30.9±4.8	-86,-24	3.3	4.2	Clowe et al. (2004)
		7.6±2.1	86,24	5.2	0.78	
Abell 2744	0.308	10.9±0.3	0,0	3.8	2.3	Boschin et al. (2006)
		3.6±0.2	48,135	4.3	1.4	
AC 114	0.312	12±0.8	0,0	3.7	2.4	Campusano et al. (2001)
		4.3±0.3	75,-75	4.2	1.5	
		2.3±0.2	80,30	4.6	1.1	
MS 1054-03	0.832	3.4±0.4	0,0	3.3	0.93	Hoekstra et al. (2000)
		3.4±0.4	50,25	3.3	0.93	
		3.4±0.4	-60,-20	3.3	0.93	

5.1. Abell 2163

This is the only cluster in this work which is simulated by a single NFW profile. A weak lensing analysis performed by Radovich et al. (2008) gives the mass we use in our simulation. There is compelling evidence that the cluster is a merger, possible ongoing, and that there are two main components (Maurogordato et al. 2008). This makes the mass distribution slightly elongated, something which we do not take into account in this work. A single elliptical NFW profile where ellipticity has been introduced or two NFW profiles might make for better models. Since at least one source in this field is relatively close to a critical line minor improvements of the model could yield drastically different magnifications of that particular source.

5.2. 1E 0657-56

Better known as the Bullet Cluster, this is the most massive cluster in this survey. It is made up of two components, a large main cluster and a smaller "bullet" subcluster. Clowe et al. (2004) fitted the main cluster to a NFW profile and measured the mass of the subcluster using aperture densitometry (Clowe et al. 2000; Fahlman et al. 1994). We use the masses to model two NFW profiles centered on the mass peaks of the two components. This field contains the brightest source in this survey which is also the most magnified one as it lies close to a critical line. Gonzalez et al. (2009) estimated magnification factors of 25 and 50 of two images of this source which lie separated by $8.6''$ near the critical line. These two images are not separable in our map so they appear as one source with a total magnification of 75. Using our lensing model we get a total magnification of 41 for this source. We use Gonzalez's value since their model is more precise.

5.3. Abell 2744

Dynamical analysis of Abell 2744 shows two superposed peaks in the velocity dispersion suggesting that it is comprised of two subclusters along the line of sight (Girardi & Mezzetti 2001). Boschin et al. (2006) estimated the mass of the cluster by assuming a NFW profile and two concentric clumps and obtained a total mass of $M = 1.4 - 1.5 \times 10^{15} M_{\odot}$ and a mass ratio of 3:1. We model this by using two concentric NFW profiles with this total mass and mass ratio. It should be noted that the 2D distribution of galaxies in Abell 2744 contains a large central peak as well as at least one other peak about $2''$ to the north-west of the center. No mass estimates of the second peak have been obtained so it is not modeled but a revised model may gain from its inclusion.

5.4. AC 144

A spectroscopic survey of galaxies lensed by AC 144 performed by Campusano et al. (2001) revised a previous lensing model by Natarajan et al. (1998). Their model is comprised of a central clump, two subclumps and a galaxy-scale component centered on each bright cluster galaxy. We model the cluster by using the velocity dispersion given by Campusano et al. as an estimate for the virial mass of each component using the virial theorem and assuming the cluster components are virialized so

$$M = \frac{3\sigma r_{\text{vir}}}{2G} \tag{54}$$

where M is the mass of a cluster component, σ is the velocity dispersion and r_{vir} is the virial radius.

The galaxy-scale components were not modelled and as before each NFW profile is spherical. An improvement on our model would take into account the ellipticity of the mass components.

5.5. MS 1054-03

At a redshift of 0.83 this is the highest redshift cluster in this survey. Hoekstra et al. (2000) constructed a mass surface density profile through weak lensing analysis and found three distinct mass concentrations coinciding with the light distribution of the cluster. By fitting SIS mass models to these three clumps they estimated the mass of each clump. We use this mass estimate as the mass for the clumps modeled as three NFW profiles. Due to the high redshift of this cluster and the dependence of the magnification on both the source and lens redshift the area in this field that is highly magnified is considerably smaller than in the other fields. In fact only a single detected source in this field has any discernible magnification.

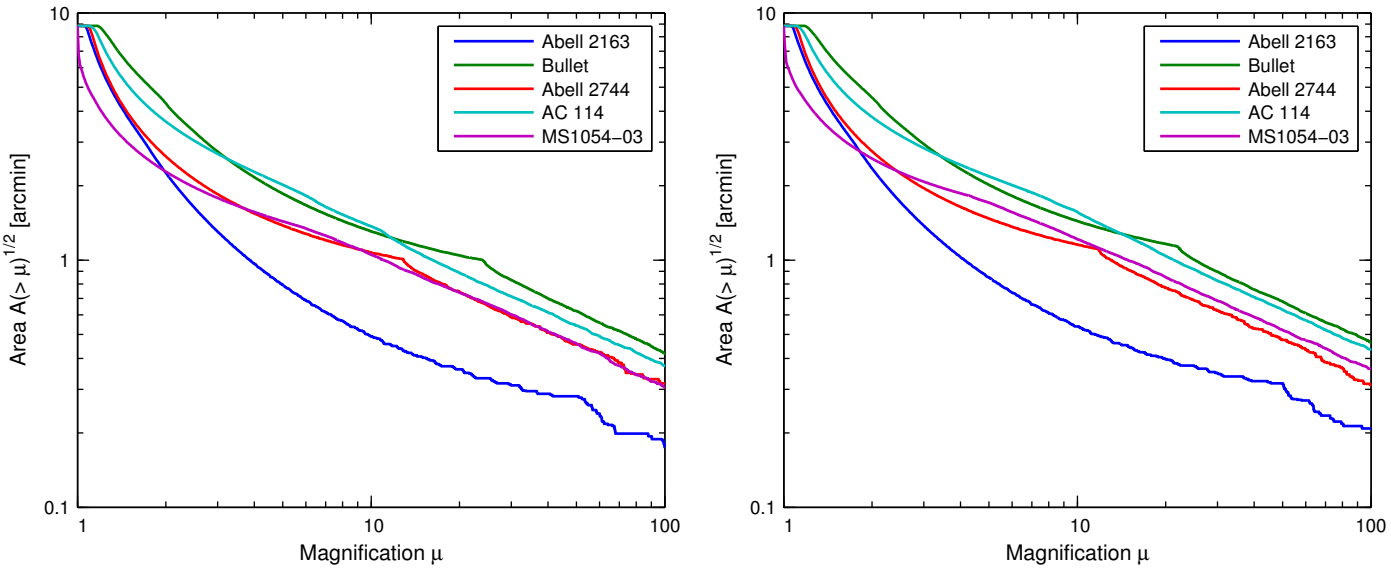

Fig. 5.—: Area with a larger magnification than μ as a function of μ. Left: $z = 2.5$. Right: $z = 4$. The redshift has little effect on the magnification except in the case of MS1054-03 which is the highest redshift cluster in this survey.

5.6. Effects of errors in mass on the magnification

An estimate was made of the effects that an error in the mass used in the model has on the magnification map, and in particular on the magnification of the detected sources in the fields. This was done by simply running the program three times, once for the given values of mass, once with adding one standard deviation of the mass of each component and once with one standard deviation subtracted from the masses.

The results can be seen in the errors in the magnification in table 2. For all sources except one, the error estimated in this way was $< 11\%$ leading us to assume that any minor uncertainties in mass will not have drastic effects on the magnification of the sources nor the resulting number counts. The exception to this is any source lying close to a critical line, in particular the magnification of the brightest

source in the Bullet Cluster field is quite sensitive to any errors in mass. This is the only source in our survey close enough to a critical line to be affected in this way and the magnification of this source has been constrained relatively well by e.g. Gonzalez et al. (2009). Any effects the error in mass may have on the magnification are most likely smaller than errors introduced by other factors such as choice in mass distribution model.

5.7. Effects of redshift on the magnification

In all the fields the source plane is assumed to be at a redshift of $z_s = 2.5$. This value was chosen as a number of spectroscopically confirmed high-redshift submm galaxies have redshifts around that value. To see what effect the redshift of the source plane has on the magnification, the computer program was run with $z_s = 4$ in all the fields, the resulting change in magnifying area can be seen in figure 5. It can clearly be seen that a change from $z_s = 2.5$ to $z_s = 4$ has little affect on the magnification in all cases except in the cluster MS 1054-03 which is also the cluster with the highest redshift in this survey. In the case of MS 1054-03 only one source lies close enough to the center of the cluster and the critical lines to be affected in any major way by the redshift and in the other clusters the redshift has a very small effect, yielding differences of about 10% in the magnification of the sources.. This is in agreement with the calculations of Johansson et al. (2010).

6. Observations and data reduction

We use observations of five fields in which high-mass galaxy clusters lie. All clusters were observed with the LABOCA instrument on the APEX telescope in Chile. We use previous observations of the Bullet Cluster from Johansson et al. (2010) in addition to observations of the clusters: Abell 2163, Abell 2744, MS1054-03 and AC114. The observations were performed by Johansson et al. (in prep) except in the case of AC114 for which data were retrieved from the ESO archive (PI. Scott).

Johansson et al. made jack-knife maps of all the fields to estimate the noise level in each map. By taking the average of histograms made from pixel-values in 500 different jack-knife maps for each field an estimate of the noise level was found. The noise level is roughly constant in the central 10 arcminutes of the maps and we will only use sources detected in that area in this work to avoid complications due to varying noise levels.

To estimate the effects of completeness of the observations Johansson et al. randomly distributed artificial sources into the jack-knife maps and ran the same source extraction algorithm they used for the observed sources. Then they constructed completeness curves for each field, these curves are displayed in figure 6.

Due to the unseen population of low flux submm galaxies the flux of each detected source is actually boosted since the flux measured is the sum of the detected source and all undetected sources in the beam (see e.g. Hogg & Turner 1998). To correct for this Johansson et al. used a method described by Coppin

et al. (2005). An underlying population of sources following a Schechter distribution is simulated. Multiplying the flux distribution of this population with the observed flux distribution as simulated by a Gaussian yields a posterior flux distribution, the maximum of which is the deboosted flux density of the source.

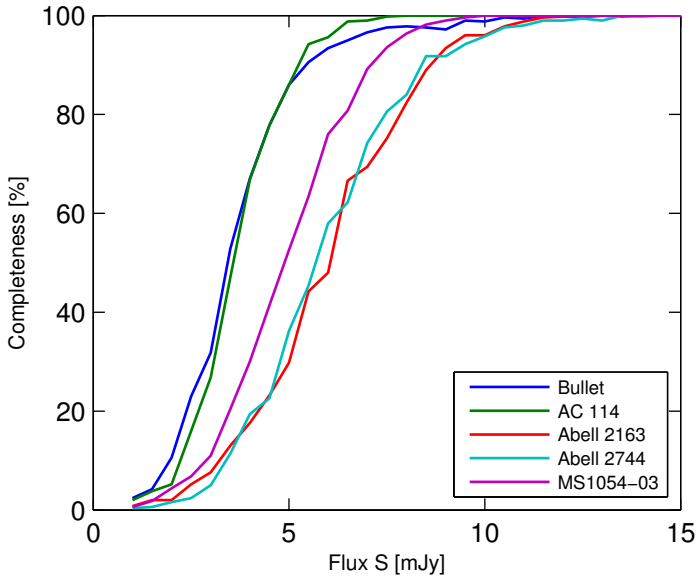

Fig. 6.—: The completeness of the five cluster fields as a function of source flux density. The completeness was calculated by inserting artificial sources int noise maps and counting the ratio of number of extracted sources against number of simulated sources.

7. Number counts

The number counts of submm is denoted by $N(> S)$, that is the cumulative number of sources per unit area with an intrinsic flux density greater than S. The number counts are complicated by the varying noise in the maps and non-uniform sensitivity. The sensitivity varies between each map and in each map due to the gravitational lensing. To account for noise fluctuations in each map we count only those sources that fall within a 10 arcminute circle in the center of each field, where the noise level is constant.

Gravitational lensing has effects on the number count of galaxies for which we have to correct. The first effect is the flux magnification which causes us to observe a higher flux from a source than we would without a lens; the intrinsic flux $S_{\rm i}$ of the source gets boosted to $S_{obs} = \mu S_{\rm i}$ where μ is the magnification factor due to the gravitational lens at the position of the source. Without correcting for this effect a source could be placed into the wrong flux bin.

The second effect is the magnification of the area in the source plane. When viewed through a gravitational lens, a certain area in the source plane corresponds to a larger area in the image plane. At each point in the image plane the ratio between the area in the source plane and the image plane is the magnification factor μ. Since the number counts are expressed as the number of sources of a certain

flux per unit area this change in area must be accounted for. Due to noise we can only reliable detect sources above a certain signal-to-noise-ratio which for a constant noise level corresponds to a minimum flux $S_{\rm min}$. In our case we assume that a source must have a signal-to-noise ratio of at least 3 to be detected. To detect a source it has to have an observed flux $> S_{\rm min}$ but the intrinsic flux can in theory be much smaller since it may be magnified above this minimum. Thus a source with a $S_{\rm i} < S_{\rm min}$ can only be detected when its image is positioned in an area of the lens plane where $\mu \geq S_{\rm min}/S_{\rm i}$ and this area, $A_{eff,l}(> S)$, is the effective area in the lens plane we are surveying for sources with this particular flux or greater. But this area in the lens plane corresponds to a smaller area in the source plane due to magnification and the effective area we are surveying in the source plane is

$$A_{eff,s}(> S) = \sum_n A_n \mu_n \tag{55}$$

where A_n is the area in the lens plane of a single area element and μ_n is the magnification of that particular element. In our case A_n corresponds to the area of one pixel and μ_n the magnification of that pixel. Thus a single detected source corresponds to number count of $1/A_{eff,s}(> S)$ sources per unit area.

By constructing magnification maps these effects can be calculated for each source and the necessary corrections made to the number count.

We must also account for the effects of incompleteness in the maps which was discussed in part 6. We do this by imagining that for each source we detect there is a number of 'phantom sources' which are in the map but are lost in the noise and thus not detected. On average for each detected source, the number of undetected sources which should have the same observed flux $S_{\rm obs}$ is $N_{\rm und} = 1/C - 1$ where C is the completeness of sources with the same flux as the detected one. Assuming that these sources are uniformly distributed in the image plane we can calculate the probability that an undetected source which would have an observed flux of $S_{\rm obs}$ has an intrinsic flux which places it in a particular flux bin. This probability is

$$P(S_{\rm int}|S_{\rm obs}) = A_{\rm obs\rightarrow int}/A_{\rm \,field} \tag{56}$$

where $A_{\rm obs\rightarrow int}$ is the area in the image plane that which has a magnification in the interval required to place a source with an observed flux $S_{\rm obs}$ into the flux bin corresponding to $S_{\rm int}$ and A_{field} is the total image plane area of the field in which the source lies.

Calculating this for each flux bin for each detected source we then distribute the hidden sources according to the probability that it would fall into each bin. The number placed in a certain bin is then $N_{\rm und} P(S_{\rm int}|S_{\rm obs})/A_{\rm field}$.

This way of distributing the undetected sources does not take into account the flux distribution of sources, i.e. that sources with lower flux have a higher number density than those with higher flux. In effect we skew the distribution of the undetected sources toward higher intrinsic flux.

In figure 7 the number counts of submm galaxies in this survey are compared with previous works. Errors were estimated using Poissonian statistics using the tabulated values from Gehrels (1986) corre-

sponding to the number of sources in each flux bin.

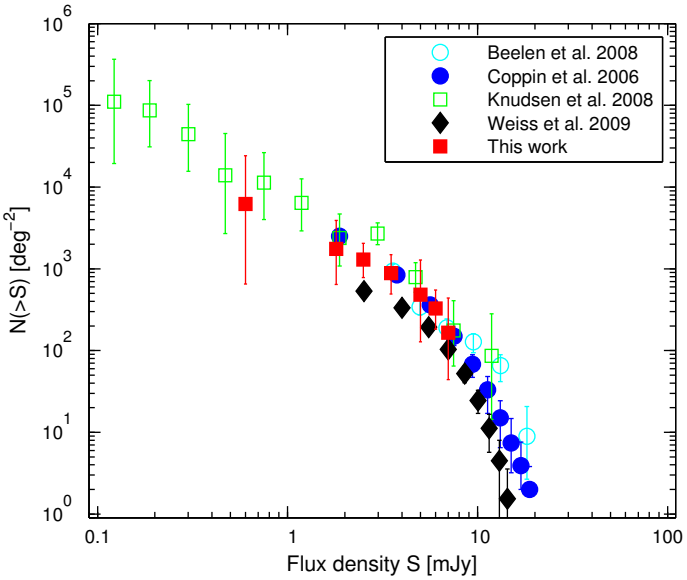

Fig. 7.—: The resulting number counts as a function of the flux density of sources along with previous results from other surveys.

8. Conclusion and discussion

In this work we have discussed the effects of gravitational lensing on sources behind massive galaxy clusters. We described a computer program that utilizes a superposition of NFW mass profiles to simulate clusters to construct magnification maps. Those magnification maps can be used to estimate the intrinsic flux of sources detected in galaxy cluster fields. The program has the advantage of being very simple and requiring only the mass, redshift and relative positions of galaxy cluster components to relatively quickly compute a magnification map. The drawbacks of the program are also part of its inherent simplicity, since real clusters are rarely made out of completely spherical components. But for an initial estimate of the magnification of detected sources it offers a simple solution.

We also discussed the effects that lensing has on number counts of submm galaxies detected behind lenses. Since number counts depend on the intrinsic magnification of the sources and the area surveyed one must account for the way that lensing boosts the flux of sources and magnifies the area. Using the magnification maps we constructed from mass models of the clusters and derived number counts from APEX-LABOCA measurements of five galaxy clusters. The number counts were adjusted to compensate for the effects of gravitational lensing. The resulting number counts are consistent with previous surveys of submm galaxies.

A number of improvements could be made to the computer program to get more reliable results. Since the magnification further away from the critical lines change slowly a variable grid could be used instead of fixed size pixels. The grid would then be finer close to the critical lines where magnification changes rapidly and coarser further away. Spherical NFW profiles do not describe real merging clusters

where the dark matter has not yet had time to completely virialize. One relatively simple improvement would be to utilize elliptical NFW profiles like those discussed in Meneghetti et al. (2003).

REFERENCES

Beelen, A., et al. 2008, A&A, 485, 645

Blain, A. W., Smail, I., Ivison, R. J., Kneib, J., & Frayer, D. T. 2002, Phys. Rep., 369, 111

Boschin, W., Girardi, M., Spolaor, M., & Barrena, R. 2006, A&A, 449, 461

Bourassa, R. R., Kantowski, R., & Norton, T. D. 1973, ApJ, 185, 747

Bryan, G. L., & Norman, M. L. 1998, ApJ, 495, 80

Bullock, J. S., Kolatt, T. S., Sigad, Y., Somerville, R. S., Kravtsov, A. V., Klypin, A. A., Primack, J. R., & Dekel, A. 2001, MNRAS, 321, 559

Campusano, L. E., Pelló, R., Kneib, J., Le Borgne, J., Fort, B., Ellis, R., Mellier, Y., & Smail, I. 2001, A&A, 378, 394

Clowe, D., Gonzalez, A., & Markevitch, M. 2004, ApJ, 604, 596

Clowe, D., Luppino, G. A., Kaiser, N., & Gioia, I. M. 2000, ApJ, 539, 540

Coppin, K., Halpern, M., Scott, D., Borys, C., & Chapman, S. 2005, MNRAS, 357, 1022

Downes, D., & Solomon, P. M. 1998, ApJ, 507, 615

Einstein, A. 1936, Science, 84, 506

Fahlman, G., Kaiser, N., Squires, G., & Woods, D. 1994, ApJ, 437, 56

Gehrels, N. 1986, ApJ, 303, 336

Girardi, M., & Mezzetti, M. 2001, ApJ, 548, 79

Gonzalez, A. H., Clowe, D., Bradač, M., Zaritsky, D., Jones, C., & Markevitch, M. 2009, ApJ, 691, 525

Hoekstra, H., Franx, M., & Kuijken, K. 2000, ApJ, 532, 88

Hogg, D. W., Baldry, I. K., Blanton, M. R., & Eisenstein, D. J. 2002, ArXiv Astrophysics e-prints

Hogg, D. W., & Turner, E. L. 1998, PASP, 110, 727

Holland, W. S., et al. 1999, MNRAS, 303, 659

Johansson, D., Horellou, C., Sommer, M. W., et al. 2010, A&A, 514, A77

Johansson, D., Sigurdarson, H., & Horellou, C. 2010, A&A, submitted

Knudsen, K. K., van der Werf, P. P., & Kneib, J. 2008, MNRAS, 384, 1611

Lima, M., Jain, B., & Devlin, M. 2010, MNRAS, 406, 2352

Maurogordato, S., et al. 2008, A&A, 481, 593

Meneghetti, M., Bartelmann, M., & Moscardini, L. 2003, MNRAS, 340, 105

Mihos, C. 1999, Ap&SS, 266, 195

Natarajan, P., Kneib, J., Smail, I., & Ellis, R. S. 1998, ApJ, 499, 600

Navarro, J. F., Frenk, C. S., & White, S. D. M. 1997, ApJ, 490, 493

Radovich, M., Puddu, E., Romano, A., Grado, A., & Getman, F. 2008, A&A, 487, 55

Sakamoto, K., Scoville, N. Z., Yun, M. S., Crosas, M., Genzel, R., & Tacconi, L. J. 1999, ApJ, 514, 68

Sanders, D. B. 1999, Ap&SS, 266, 331

Schneider, P., Kochanek, C., & Wambsganss, J. 2006, Gravitational Lensing: Strong, Weak and Micro: Saas-Fee Advanced Course 33 (Saas-Fee Advanced Courses) (1 ed.) (Springer)

Schneider, P., & Weiss, A. 1986, A&A, 164, 237

Takada, M., & Jain, B. 2003, MNRAS, 344, 857

Weiß, A., et al. 2009, ApJ, 707, 1201

Table 2:: Source catalogue.

Submm source name	$S_{\rm obs}$ [mJy]	$S_{\rm int}$ [mJy]	μ
AC 114			
SMM J225835.0-344453	8.0±1.4	7.1	1.13
SMM J225835.7-344812	3.1±2.0	1.27	1.36
SMM J225844.7-345131	10.6±1.2	8.4	1.26
SMM J225905.9-344639	4.2±1.2	3.7	1.14
Abell 2744			
SMM J001400.2-302447	6.8±1.6	6.2	1.09
SMM J001406.3-301942	6.1±1.5	4.9	1.23
SMM J001407.7-302439	4.8±1.3	4.1	1.18
SMM J001408.6-302142	8.0±1.3	5.1	1.58
SMM J001418.3-302525	3.3±1.6	2.9	1.16
SMM J001423.4-302018	5.5±1.6	3.5	1.54
MS 1054-03			
SMM J105643.7-033543	5.3±1.7	5.2	1.01
SMM J105650.8-034046	6.5±1.6	6.4	1.01
SMM J105656.4-033622	6.5±1.3	4.4	1.47
SMM J105703.2-034135	6.8±1.7	6.7	1.01
SMM J105703.7-033309	6.5±1.8	6.5	1.00
Abell 2163			
SMM J161525.8-060803	4.3±3.5	3.8	1.12
SMM J161541.2-060817	–	–	1.57
SMM J161547.7-060948	6.4±2.3	3.0	2.14
SMM J161553.1-060655	4.5±2.3	2.9	1.54
1E 0657-56			
SMM J065751.4-560112	9.7±3.0	8.9	1.09
SMM J065813.4-555732	4.2±1.0	2.8	1.51
SMM J065819.4-555830	7.7±0.9	7.22	1.21
SMM J065822.9-560041	3.8±1.3	2.9	1.31
SMM J065824.0-555723	4.7±1.0	2.1	2.19
SMM J065824.5-555512	14.7±1.0	9.3	1.57
SMM J065825.5-555640	6.4±1.0	2.8	2.24
SMM J065827.3-560116	8.0±1.3	6.3	1.27
SMM J065828.9-555349	8.6±1.2	6.5	1.32
SMM J065833.7-555441	3.6±1.2	2.4	1.52
SMM J065837.6-555705	48.0±1.3	0.6	75
SMM J065845.6-555848	5.5±1.1	2.9	1.87
SMM J065846.6-560212	4.6±2.5	3.8	1.19
SMM J065853.2-560046	6.4±1.6	5.0	1.27
SMM J065853.7-555543	4.5±1.2	3.0	1.49
SMM J065856.0-555652	4.4±1.3	3.0	1.47
SMM J065901.3-555218	11.9±2.1	8.6	1.13
SMM J065915.6-560108	–	–	1.11

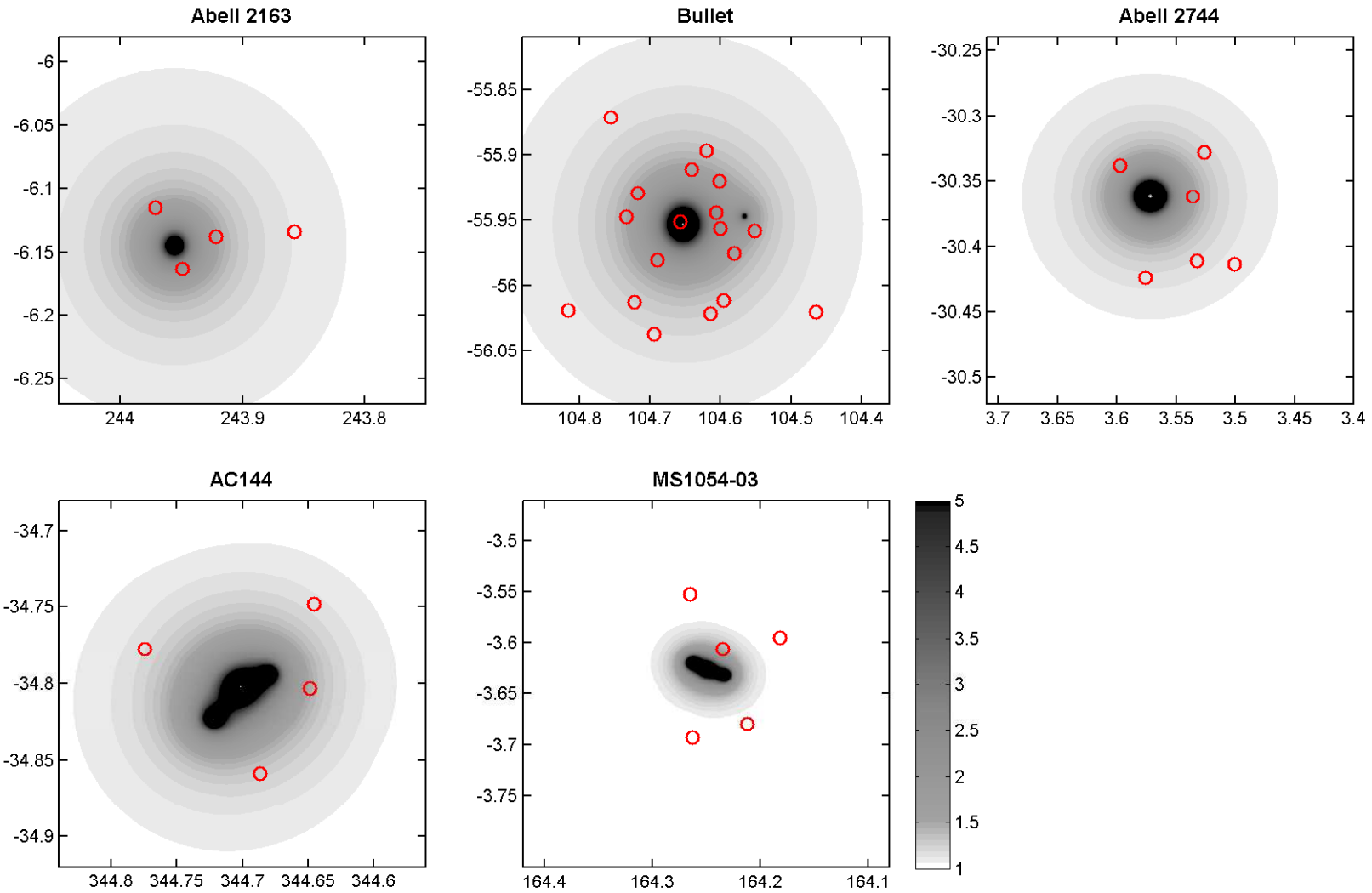

Fig. 8.—: Magnification maps of the five fields discussed in this work. The red circles indicate the positions of the detected submm sources. The magnification is capped at 5 in order to make the maps more readable. Right ascension is along the horizontal axis and declination along the vertical axis. Both axes are in units of degrees.